Measurement of Residual Stress Using Interferometric Moiré: A New Insight

by R. C. Schwarz, L. M. Kutt and J. M. Papazian

ABSTRACT—The use of interferometric moiré and hole drilling to determine residual stress has been well reported and accepted for stress fields whose principal directions can be predicted well enough to permit the moiré grids to be aligned with the principal strain axes. When the principal strains do not align themselves with the grid axes, a third strain component can be obtained by working with the diagonal pitch of the moiré grid, but this requires resetting the optical bench to the lower frequency. Diffraction efficiency is lost, with an additional loss in sensitivity. In this paper, the authors determine the shear strain component by observing the rotation of the moiré fringes in close proximity to the hole. The results of experiments on a specimen containing a model residual stress distribution are presented and compared with the theoretical prediction. Finally, the isothetic contours, based on elastic theory, were computed and plotted for several cases to verify this proposition. These results and the expected residual stress distribution are also compared to the experimentally obtained moiré fringes.

KEY WORDS—Residual stress, moiré interferometry, hole drilling

Fabrication and processing operations often introduce residual stresses to structural components. Operations involving localized heating (e.g., welding), differential thermal expansion (e.g., heat treatment of composites) or plastic deformation (e.g., forming) create internal stresses that may be retained in the finished component. These stresses can be desirable (e.g., cold-worked holes) or undesirable (e.g., weld cracking). Measurement of the magnitude and direction of residual stresses is often necessary because the stresses can influence the service life of a component. X-ray diffraction, ultrasonic birefringence, Barkhausen noise and mechanical techniques are all used to measure residual stresses.[1] Of the mechanical techniques, hole drilling is routinely used.[2]

In the hole-drilling method, a small, shallow hole ($\approx$ 1 mm diameter by 1.5 mm deep) is drilled in the sample, and the local displacement of the surface, in response to the material removal, is measured, usually with strain gages. Because drilling the hole releases local stresses, the adjacent surface undergoes displacements in response to the new stress equilibrium, and measurement of these displacements allows the calculation of the state of stress that existed prior to the drilling operation. Displacements and strains in the direction normal to the surface are usually ignored in this measurement. The ASTM standard fully describes the use of strain gages for this measurement. However, the use of strain gages is disadvantageous. Displacements cannot be measured at the edge of the hole, and the location of the hole is critical. The strain gages measure strain over a particular gage length, which is usually several diameters away from the edge of the hole.

Moiré interferometry[3–5] is an alternate technique for the measurement of the surface displacements caused by hole drilling. In this technique, a fine, linear diffraction grating is attached to the sample surface, the hole is drilled, and the surface displacement is measured from the moiré fringe pattern created by interference between the sample grating and a reference grating.[6,7] The advantages are that displacements can be measured at the edge of the hole and the location of the hole is not critical. The technique is also insensitive to out-of-plane displacement. The sensitivity of the displacement measurement depends on the line density of the grating according to the relationship

$$u_x = \frac{1}{f} N_x, \tag{1}$$

where u_x is the displacement in the x-direction, f is the frequency of the reference grating and N_x is the fringe order. For instance, with a reference grating frequency of 2400 lines/mm, the sensitivity of the displacement measurement is 0.417 μm per fringe order. The fringe order can be interpolated to one-tenth of an order if necessary, this displacement would represent a strain of approximately 4×10^{-5} if it were measured over the hole diameter of 1 mm (i.e., $e = \Delta l/l = 0.1 \times 0.417 \mu m/mm$). For typical aluminum alloys, an elastic strain of this magnitude represents a stress of approximately 3 MPa (0.4 ksi), which is excellent sensitivity. The relationship between the principal residual strains (ε_1 and ε_2) and the strain components obtainable from the moiré fringes (ε_x, ε_y and ε_{xy}) are given by

$$\varepsilon_{1,2} = \frac{\varepsilon_x + \varepsilon_y}{2} \pm \sqrt{\left(\frac{\varepsilon_x - \varepsilon_y}{2}\right)^2 + \left(\frac{\gamma_{xy}}{2}\right)^2}. \tag{2}$$

When an assumption of a state of elastic plane stress is made, the relationship between the principal strains and the corresponding principal stresses is given by[8]

$$\sigma_1 = \frac{E}{1 - \nu^2} (\varepsilon_1 + \nu \varepsilon_2) \tag{3}$$

R. C. Schwarz (SEM Member) is a Senior Technical Specialist, L. M. Kutt is a Senior Technical Specialist, and J. M. Papazian is a Technical Manager, Northrop Grumman, Bethpage, NY 11714-3581.

Original manuscript submitted: September 10, 1998.
Final manuscript received: April 25, 2000.

$$\sigma_2 = \frac{E}{1-\nu^2}(\varepsilon_2 + \nu\varepsilon_1). \quad (4)$$

When the moiré grids are aligned with the principal strain directions, there is no shear component (γ_{xy}), and the principal strains are obtained by the ε_x and ε_y strain components obtained from the moiré system with the reference fringes aligned with the specimen grid axes. When the principal strains do not align themselves with the grid axes, a third strain component can be obtained by working with the diagonal pitch of the moiré grid. For our optical system, this requires resetting the optical bench to the lower frequency. Doing this results in a loss of diffraction efficiency, producing poorer images, and the reduced pitch produces a loss in sensitivity.[9] It should be noted that other more complex optical arrangements can be employed to overcome the need to reset the optical bench.[9]

During the course of our experiments, we noticed that when the grid was not aligned with the principal strain axes, the moiré fringes rotated in the immediate vicinity of the hole boundary. This led to an investigation into the relationship between moiré fringe orientation and principal strain direction. This paper will present the results of this investigation and show that the complete state of stress can be determined from an analysis of the two orthogonal moiré fringe images.

Experimental Procedure

The test specimen chosen for this experiment was an aluminum disk (7075-T6, 100 mm outer diameter × 25 mm inner diameter × 12.5 mm thickness) with an interference plug inserted into the center hole. A diametral interference of 0.059 mm was chosen to provide internal stresses that were entirely elastic. A 25 mm × 25 mm grid with a density of 600 lines/mm was bonded to the right-hand side of the disk, and a 25 mm × 25 mm grid with a density of 1200 lines/mm was bonded to the left-hand side of the disk. A number of holes were then carefully drilled into the disk at locations where the grids were aligned with the principal strain axes ($\gamma_{xy} = 0$) and at locations in which a general state of strain would exist ($\gamma_{xy} \neq 0$). Figure 1 shows the gridded disk and test holes. Table 1 lists the coordinates of the holes in the test disk.

The application of interferometric moiré and hole drilling to the determination of residual stress involves several distinct tasks. These can be conveniently separated as (1) preparation of specimen grids, (2) specimen gridding, (3) hole drilling, (4) specimen interrogation and (5) determination of residual stresses from interference fringes.

Preparation of Specimen Grids

The preparation of the master grids used an optical setup similar to that shown in Fig. 2, except that an unexposed photographic plate was placed on the rotary stage instead of the test specimen. The plate was first exposed with the stage set at 0 deg. The stage was rotated precisely 90 deg, and the plate was exposed a second time. The result is a crossed grating with the chosen frequency. The frequency of the test grid was established by first placing a 300 lines/mm ruled grating at the location where the photographic plate would be exposed. The mirrors are coarsely adjusted by aligning them so that the first-order diffracted beams from each leg of

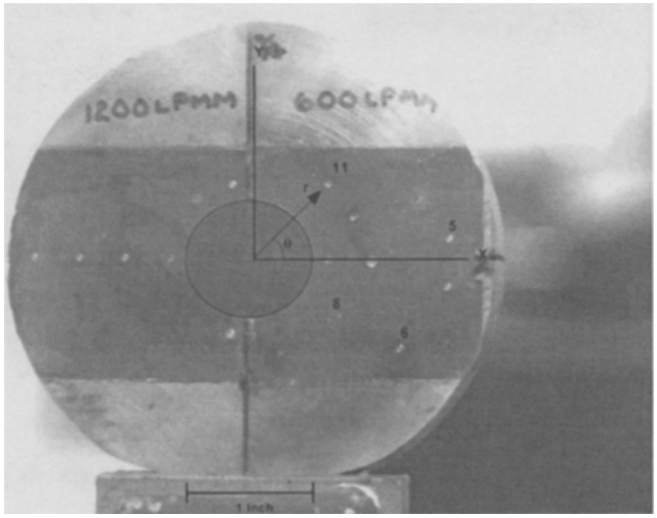

Fig. 1—Interference disk with moiré grids and drilled holes

the light path coincide. Final adjustment is made by imaging the resulting moiré created by a reference grating and the interfering laser beams on a screen, then fine tuning the mirrors to produce as clear a field as possible. This technique allows the interference fringe frequency to be adjusted to the desired frequency, 600 lines/mm, with an error of less than one fringe per 25 mm. The same procedure was followed later in the project, using a 600 lines/mm ruled grating to produce master gratings with a density of 1200 lines/mm.

Specimen Gridding

The application of the grid to the test specimen followed the procedures published by Post.[3] Basically, the exposed and developed crossed grating was coated with a thin gold plating by vapor deposition. This was then bonded to the test specimen using a two-part epoxy adhesive. After the epoxy adhesive cured, the photographic plate was pried off the test specimen. The bond between the gold plating and the photographic emulsion was generally weaker than the bond between the epoxy and the gold plating, and the prying off of the photographic plate left the gold plating with the crossed phase grating on the surface of the test specimen. As can be seen in Fig. 1, the test specimen has been instrumented with two gratings. Initially, the specimen was gridded with a 600 lines/mm grating. After analyzing a number of holes, we wanted to know if better accuracy could be obtained with a grating of higher density. Thus, the second side of the test specimen was instrumented with a grating of 1200 lines/mm.

Hole Drilling

The residual stresses are made apparent by drilling a small diameter hole into the disk through the phase grating. The residual stresses in the material surrounding the hole cause this material to deform locally in response to the new, stress-free boundary at the edge of the hole. It is important that the drilling operation be done in such a manner as to avoid the introduction of new residual stresses produced by the drilling, or distortion of the gold-plated epoxy phase grating by heat-up during drilling. The following process produced holes with a sharp fringe definition at their boundaries. The hole was started with a number 1 center drill. This was followed

TABLE 1—COORDINATES OF HOLES IN TEST DISK

Hole Number	Diameter (mm)	X	Y	R	θ
1	1.63	9.53	0.00	9.53	0.0
2	1.60	15.88	0.00	15.88	0.0
3	2.49	25.40	0.00	25.40	0.0
5	1.63	35.05	12.7	37.08	20.2
6	1.63	31.75	−19.05	37.08	−31.0
8	1.63	19.25	−11.13	22.23	−30.0
10	1.63	6.83	−19.38	20.55	−70.6
11	1.63	16.31	15.62	22.58	43.8
12	1.63	41.05	−5.54	41.43	−6.5
13	1.63	41.33	4.70	41.58	7.7
14	1.63	−15.88	0.00	15.88	0.0
15	1.63	−25.40	0.00	25.40	0.0
16	1.63	−35.05	0.00	35.05	0.0
18	1.63	−10.21	0.00	10.21	0.0
19	1.63	−3.18	15.88	16.18	101.0

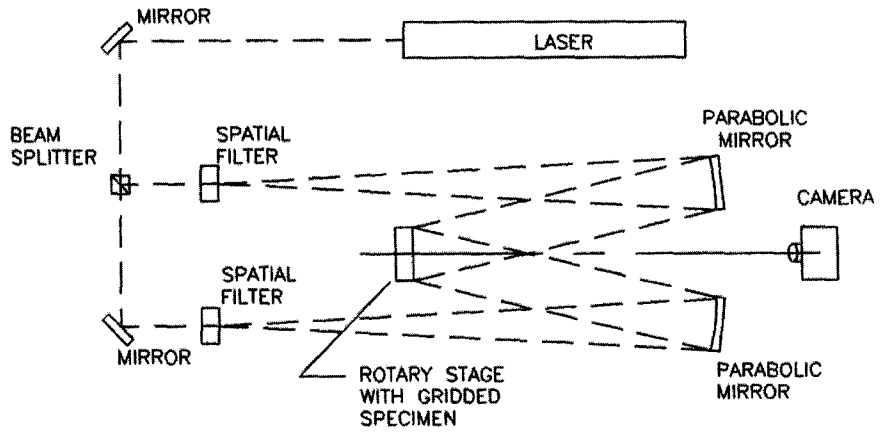

Fig. 2—Optical arrangement of the interferometer

TABLE 2—SUMMARY OF RESIDUAL STRESS MEASUREMENTS IN A SAMPLE OF ANNEALED 7075 ALUMINUM

Radial Stress (MPa)	Tangential Stress (MPa)
12.91	10.92
−9.40	−20.43
8.90	0.11

by peck drilling with a number 55 drill (1.32 mm diameter). The peck drill was set for 0.13 mm depth increments to a final depth of 2.54 mm. This was followed by peck end milling using a 1.60 mm diameter end mill. Again, the peck increments were set for 0.13 mm depth increments to a final depth of 1.78 mm. All drilling operations were accomplished at 1500 rpm with water soluble oil cooling. Finally, the surface was rinsed with methanol and blown dry with shop air. To validate our drilling procedure, which was performed on a shop type milling machine, a sample of 7075 aluminum in the annealed state (residual stress free) was grated. Three holes were drilled and analyzed. Table 2 presents the results of these measurements. The average error for the six stress components was 10.4 MPa, with a standard deviation of 6 MPa. There was no systematic error that would imply the errors were produced by a residual stress created by the drilling process.

Specimen Interrogation

An optical table, shown schematically in Figure 2, was set up using a helium- neon laser with a wavelength of 632.8 nm. The optical bench was set such that the angle between the interfering beams produced a vertical interference pattern with a density of 1200 or 2400 lines/mm. The fringe pattern of the interrogation interferometer was set for twice the frequency of the pattern used to produce the phase grating on the test specimen, since the optical moiré pattern was created between the first-order diffracted beam from the sample grating and the optical fringe pattern created by the intersecting beams in front of the sample. The interrogating interferometer was calibrated with precision 600 or 1200 lines/mm linear phase gratings. The test specimen was positioned in the interferometer on a vertically mounted, motor-driven, rotary stage. The x-displacement fringes and y-displacement fringes were formed separately after rotation of the stage by 90 deg. The interference fringes were viewed and recorded by a CCD video camera. A suitably equipped desktop computer was linked to the CCD camera to permit storage, printing and processing of the camera image.

Determination of Residual Stresses

When the principal residual strains are aligned with the orthogonal rulings of the phase grating, the shear strain (γ_{xy})

equals zero, and the two strain components obtained from the x-displacement and y-displacement images are sufficient to determine the principal residual strains. Let us consider the drilled hole as the equivalent of a pair of overlapping, orthogonal strain gages, with a gage length equal to the diameter of the hole, from which we can extract two displacements, u_x and u_y. The change in hole diameter was converted to engineering strains, ε_x and ε_y, by dividing by the original hole diameter. From these, the two principal residual stresses were found [eqs (1)-(4)]. In principle, there should be no fringes visible in regions where there is no local displacement, that is, far from the hole. However, it is apparent from Figs. 3(a) and 3(b) that a uniform fringe pattern often covers the field of view and is distorted in the vicinity of the hole. The background fringe pattern is caused by a slight mismatch between the fringe spacing on the specimen grating and the optical reference pattern. The quantity of mismatch fringes that would be present in the gage length used to calculate strain must be subtracted out during the computation process. The first step, then, is to determine the sign of the mismatch fringes, that is, whether the mismatch fringes represent an apparent compressive (negative) or an apparent tensile (positive) strain. The test specimen is mounted on a precision rotary stage, and this determination is accomplished by physically rotating the specimen a small amount and observing the direction of rotation of the fringes, as shown in Fig. 4. For the interferometer system shown in Fig. 2, if the moiré fringe pattern rotates in the same direction as the specimen, then the density of the specimen grating is higher than the reference grating.[11] The result is an apparent compression, and the mismatch fringes are assigned increasingly negative orders as the coordinate becomes more positive [x when determining ε_x as shown in Fig. 3(a), and y when determining ε_y as shown in Fig. 3(b)]. The mismatch fringes shown in Figs. 3(a) and 3(b) were determined to be compressive fringes. An accurate value of the image magnification is also required to analyze the fringe pattern. This was obtained by including a reference scale in the image as shown in Fig. 5.

As noted previously, when the principal strains are not aligned with the orthogonal rulings of the phase grating, the two strain components obtained from the x-displacement and y-displacement images are not sufficient to determine the principal residual strains. A third piece of data is required. Let us examine closely the fringe images immediately adjacent to the hole boundary in Figs. 6(a) and 6(b). In Fig. 6(a) (the x displacements), we observe that between the $+1$ and -3 fringe orders, the fringes are discontinuous through the hole. If we mark the intersections of the first discontinuous fringe on each side of the hole with the hole boundary (i.e., locate the points of algebraic maximum and minimum tangential displacement) and draw a diametral line bisecting these marks, there appears to be a symmetry to the fringe intersections with the hole boundary. In Fig. 6(a), this line is at an angle of -27 degrees to the x-axis. If we repeat this process for the y displacements, we observe the same phenomena for the -1 to $+1$ fringes. In Fig. 6(b), the bisecting line is at an angle of -32 deg to the x-axis. The average of the two angles is -29.5 deg. The measurement of fringe rotation was done manually, using a protractor, with an accuracy of approximately one-quarter degree. It appears that this angle is the same as the location angle of the drilled hole, relative to the x, y coordinate system established by the moiré grating bonded to the surface of the disk. Consider the circular disk

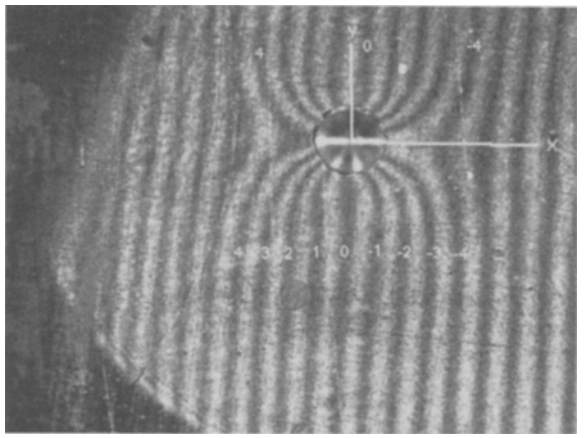

(a)

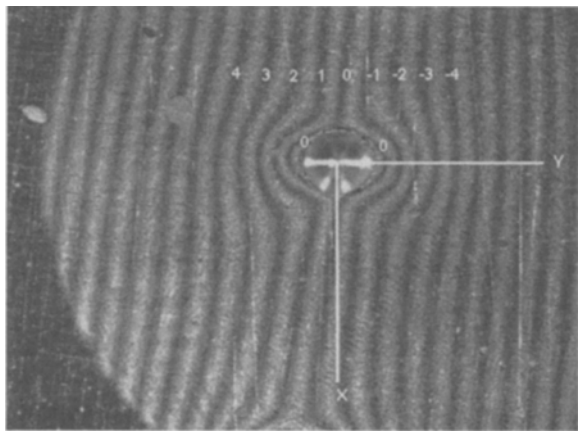

(b)

Fig. 3—Moiré fringe image of the (a) x displacements (radial), hole 2, and (b) y displacements (tangential), hole 2

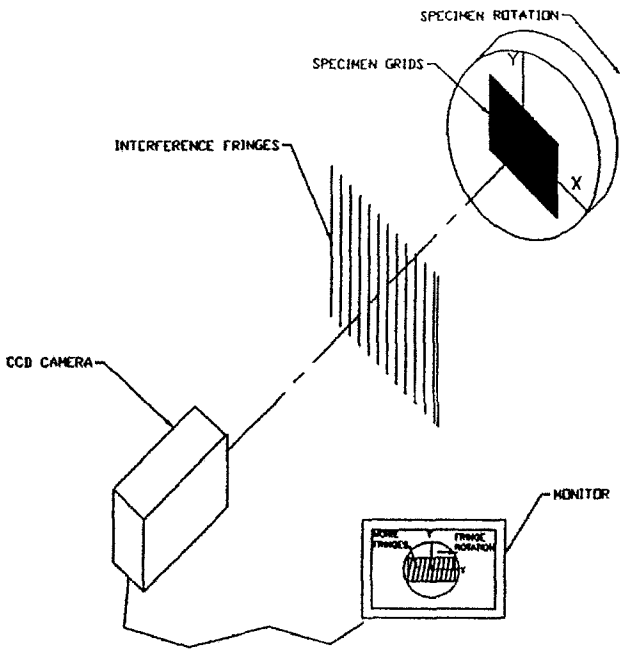

Fig. 4—Determination of moiré fringe signs

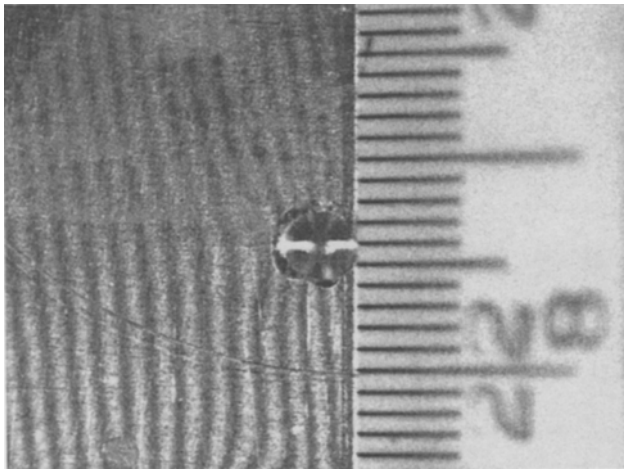

Fig. 5—CCD camera image, camera magnification

of outer radius C, with a concentric circular hole of radius B (see Fig. 7). A circular plug of radius $B + \Delta$ was shrunk into the disk, Δ being the magnitude of the radial interference. The result is a radial residual stress field σ_1 and a tangential residual stress field σ_2 throughout the test specimen.[10] Note that σ_1 and σ_2 are also the principal stresses.

In the disk, for $B \leq R \leq C$, where R is the radial distance from the center of the disk, the theory of elasticity gives

$$\sigma_1 = \frac{E\Delta}{2C} \cdot \frac{B}{C} \cdot \left(1 - \frac{C^2}{R^2}\right) \tag{5}$$

$$\sigma_2 = \frac{E\Delta}{2C} \cdot \frac{B}{C} \cdot \left(1 + \frac{C^2}{R^2}\right). \tag{6}$$

Both σ_1 and σ_2 are functions of the distance R from the center but are independent of the angular coordinate. The theoretical principal residual stresses cited in this paper were calculated using eqs (5) and (6). Thus, the theoretical principal strain angle will equal the polar coordinate angle of the hole, and the angle of fringe symmetry is equal to the principal strain angle.[10] If the angle of fringe symmetry, as determined from the moiré images, is used with the x and y strain components to calculate the shear strain [eq (7)], then the principal strains can be determined [eq (2)]. Once the principal strains are found, the principal residual stresses can be determined from eqs (3) and (4):

$$\gamma_{xy} = \{\varepsilon_x - \varepsilon_y\} \tan\theta. \tag{7}$$

This process is best illustrated in Table 3, which is the solution of the principal residual stresses for hole 8 [Figs. 6(a) and 6(b)]. Following this procedure, the symmetry angles for the off-axis test holes in the specimen were measured and compared with their actual location in the specimen. The results are given in Table 4 and show good correlation.

Computational Simulation of Moiré Fringe Patterns

To further test this hypothesis, a study was conducted in which the moiré fringe patterns were simulated and plotted mathematically.

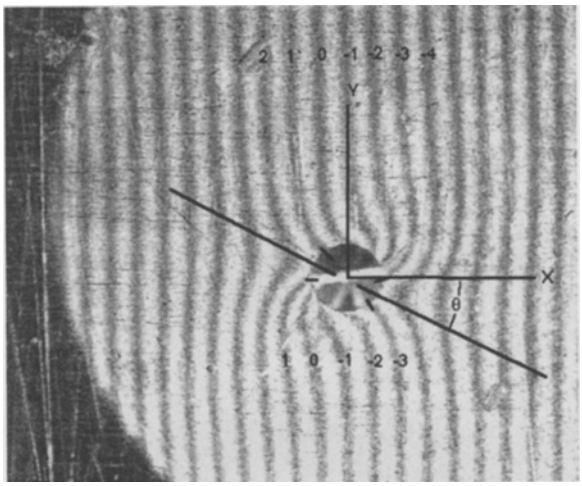

(a)

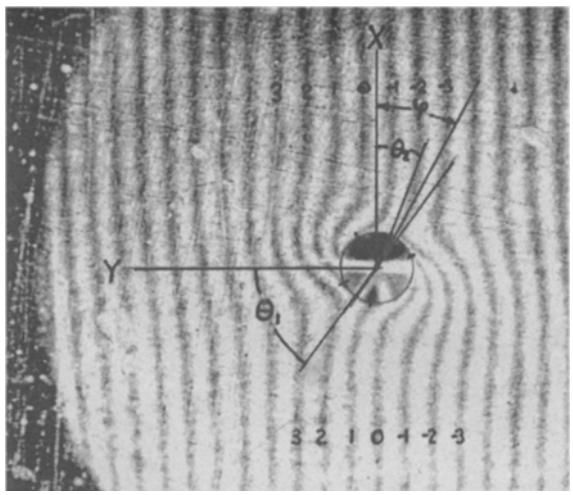

(b)

Fig. 6—Moiré fringe image of the (a) x displacements (radial), hole 8, and (b) y displacements (tangential), hole 8

Equations for the Infinite Plate with a Hole

The solution for the stress fields for an infinite plate with a hole under uniaxial tension σ_1 (i.e., $\sigma_2 = 0$) is obtained from the linear theory of elasticity.[12] Using the equations for the stress fields, along with a coordinate transformation, a change of variables and the principle of superposition, the stress fields for the general biaxial problem, in which both σ_1 and σ_2 are nonzero, are easily solved. The radial stress σ_r, tangential stress σ_θ and shear stress $\tau_{r\theta}$ are

$$\sigma_r = \frac{(\sigma_1 + \sigma_2)}{2} \cdot \left[1 - \frac{b^2}{r^2}\right] + \frac{(\sigma_1 - \sigma_2)}{2} \cdot \left[1 - \frac{b^2}{r^2}\right] \cdot \left[1 - \frac{3b^2}{r^2}\right] \cdot \cos 2\theta \tag{8}$$

$$\sigma_\theta = \frac{(\sigma_1 + \sigma_2)}{2} \cdot \left[1 + \frac{b^2}{r^2}\right] - \frac{(\sigma_1 - \sigma_2)}{2} \cdot \left[1 + \frac{3b^4}{r^4}\right] \cdot \cos 2\theta \tag{9}$$

TABLE 3—SOLUTION OF PRINCIPAL RESIDUAL STRESSES FOR HOLE 8

General data			
Image hole diameter =	19.56		
Actual hole diameter =	1.60 mm		
Image magnification =	12.22		
Moiré density (lines/mm) =	1200		
Moiré sensitivity (mm/fringe) =	8.33 E - 04		
Young's modulus =	70.97 GPa		
Poisson's ratio =	0.33		
X-displacement image			
Number of mismatch fringes =	−10		
Mismatch image distance =	80.01 mm		
X Mismatch (fringes/mm) =	−0.12498		
X− fringe number =	1		
X+ fringe number =	−3		
X displacement (mm) =	−0.001296		
X strain =	−0.00081		
Y-displacement image			
Number of mismatch fringes =	−10		
Mismatch image distance =	74.17 mm		
Y Mismatch (fringes/mm) =	−0.13483		
Y− fringe number =	−0.2		
Y+ fringe number =	0.5		
Y displacement (mm) =	−0.001614		
Y strain =	0.0010291		
Principal strain angle			
Average principal strain angle =			
Shear strain =			
Principal strains			
ε 1 =	0.001144		
ε 2 =	−0.000946		
Principal stresses (MPa)	Experiment	Theory	Error
σ 1 =	66.29	64.71	−1.58
σ 2 =	−45.23	−43.92	1.31

TABLE 4—COMPARISON OF EXPERIMENTALLY MEASURED PRINCIPAL STRAIN ANGLES WITH A THEORETICAL PRINCIPAL STRAIN ANGLE

Hole Number	Predicted Principal Strain Angle	Measured Angle of Symmetry from Moiré Images	Principal Strain Angle from Calculated Plots
5	20	23	20
6	−31	−29	−31
8	−30	−33	−30
11	44	45	44

$$\tau_{r\theta} = -\frac{(\sigma_1 - \sigma_2)}{2} \cdot \left[1 - \frac{b^2}{r^2}\right]\left[1 + \frac{3b^2}{r^2}\right] \cdot \sin 2\theta, \quad (10)$$

where r is the radial distance from the center of the hole, θ is the angular polar coordinate and b is one-half of the diameter of the hole.

Equations (8)-(10) are combined with the isotropic, linear, elastic, plane stress version of Hooke's law and the geometrically linear strain-displacement relations, and the resulting equations are integrated. This results in the displacement fields $u_r^{(1)}$ and $u_\theta^{(1)}$ in the r, θ polar coordinate system:

$$u_r^{(1)} = b \cdot \frac{\sigma_1 + \sigma_2}{2E} \cdot \left[(1-\nu)\frac{r}{b} + (1+\nu)\frac{b}{r}\right] + b \cdot \frac{\sigma_1 - \sigma_2}{2E} \cdot \left[(1+\nu)\frac{r}{b} + 4\frac{b}{r} - (1+\nu)\frac{b^3}{r^3}\right] \cdot \cos 2\theta \quad (11)$$

$$u_\theta^{(1)} = -b \cdot \frac{\sigma_1 - \sigma_2}{2E} \cdot \left[(1+\nu)\frac{r}{b} + 2(1-\nu)\frac{b}{r} + (1+\nu)\frac{b^3}{r^3}\right] \cdot \sin 2\theta, \quad (12)$$

where $u_r^{(1)}$ is the displacement in the radial direction and $u_\theta^{(1)}$ is the displacement in the tangential direction. The superscript (1) is used to distinguish this solution from the one presented in the following section.

A local, Cartesian x, y coordinate system can be identified, which has its origin at the center of the drilled hole; its x-axis is parallel to and pointing in the same direction as the X-axis of Fig. 8 and its y-axis is parallel to and pointing in the same direction as the Y-axis of Fig. 8. The transformation equations relating the local polar coordinate system r, θ of the drilled hole to this local, Cartesian x, y coordinate system are

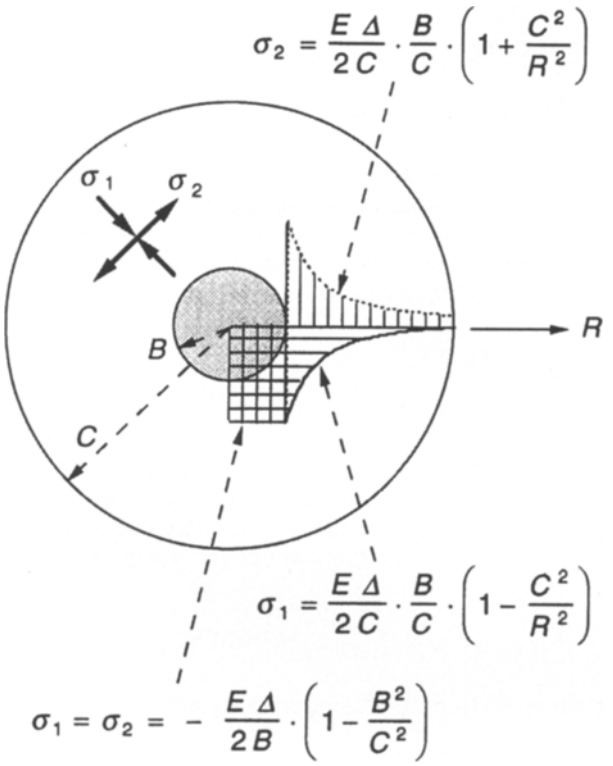

Fig. 7—Residual stress fields in a circular, shrink-fit test specimen

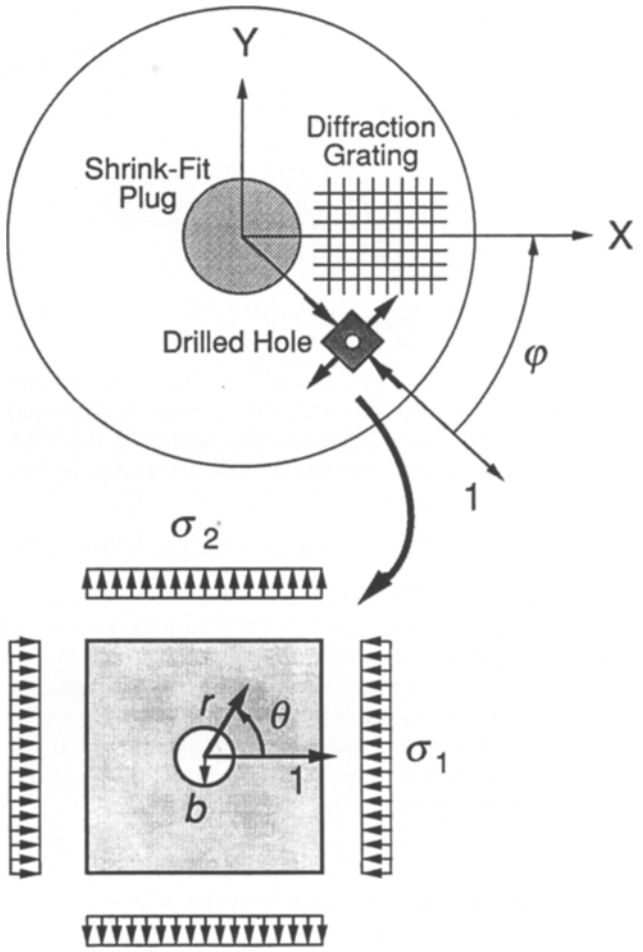

Fig. 8—Shrink-fit test specimen and drilled hole coordinate systems

$$x = r\cos(\theta - \varphi) \tag{13}$$

$$y = r\sin(\theta - \varphi). \tag{14}$$

Note that φ amounts to being the angle of orientation of the axes of principal stress. The displacements $u_x^{(1)}$ and $u_y^{(1)}$ in the directions of the furrows of the diffraction grating—that is, in the x- (or X-) direction and the y- (or Y-) direction, respectively—can be calculated from the following transformation equations:

$$u_x^{(1)} = u_r^{(1)} \cdot \cos(\theta - \varphi) - u_\theta^{(1)} \cdot \sin(\theta - \varphi) \tag{15}$$

$$u_y^{(1)} = u_r^{(1)} \cdot \sin(\theta - \varphi) + u_\theta^{(1)} \cdot \cos(\theta - \varphi). \tag{16}$$

Equations for the Infinite Plate without Any Holes

The diffraction grating is applied to the test specimen, which has an existing state of residual stress. In other words, the grating is applied after the plug is shrink fitted into the disk of the test specimen, and therefore the grating does not manifest the displacements that any point in the disk undergoes due to the introduction of residual stresses. What the grating will detect are the additional displacements introduced when the small hole is drilled and residual stresses in the vicinity of the hole are redistributed. However, the displacement fields of eqs (11), (12), (15) and (16) are absolute displacements, not the additional, relative displacements measured by the diffraction grating. Thus, what is required are the absolute displacement fields that the points in the area of the hole make with the introduction of residual stresses, but before any holes are drilled.

The solution is simple. Using the notation defined previously, the σ_x, σ_y and τ_{xy} stresses are, for an infinite plate without any holes and with a constant, biaxial stress field σ_1 and σ_2,[13]

$$\sigma_x = \sigma_1\cos^2\varphi + \sigma_2\sin^2\varphi \tag{17}$$

$$\sigma_y = \sigma_1\sin^2\varphi + \sigma_2\cos^2\varphi \tag{18}$$

$$\tau_{xy} = (\sigma_2 - \sigma_1)\sin\varphi\cos\varphi. \tag{19}$$

Combining eqs (17)-(19) with Hooke's law and the strain-displacement relations and integrating, the corresponding displacement fields $u_x^{(2)}$ and $u_y^{(2)}$ are

$$u_x^{(2)} = \left[\frac{\sigma_1 - \nu\sigma_2}{E}\cos^2\varphi + \frac{\sigma_2 - \nu\sigma_1}{E}\sin^2\varphi\right]x + \left[\frac{\sigma_2 - \sigma_1}{2E}(1+\nu)\sin 2\varphi\right]y \tag{20}$$

$$u_y^{(2)} = \left[\frac{\sigma_2 - \sigma_1}{2E}(1+\nu)\sin 2\varphi\right] x + \left[\frac{\sigma_1 - \nu\sigma_2}{E}\sin^2\varphi + \frac{\sigma_2 - \nu\sigma_1}{E}\cos^2\varphi\right] y. \quad (21)$$

Using eqs (11), (12), (15), (16), (20) and (21), the displacements u_x and u_y that the diffraction grating sees are

$$u_x = u_x^{(1)} - u_x^{(2)} \quad (22)$$

$$u_y = u_y^{(1)} - u_y^{(2)}. \quad (23)$$

The importance of the $u_x^{(2)}$ and $u_y^{(2)}$ correction terms may seem obvious, but initially this subtle point was missed, and eqs (11)-(16) were used alone in calculating the residual stresses from the experiments and obtaining the iso-displacement contour plots.

Iso-displacement Contour Plots and Optical Mismatch

In summary, eqs (22) and (23) combine the solution for an infinite plate with a hole [eqs (11)-(16)] with the solution of an infinite plate without a hole [eqs (20) and (21)]. The resulting combined solution basically defines two complicated functions u_x and u_y in the independent variables x and y (or r and θ) and in terms of the parameters E, ν, b, φ, σ_1 and σ_2. Iso-displacement contour lines in the x-y plane for given values of displacement $\alpha_1, \alpha_2, \ldots$ are defined by

$$u_x(x, y) = \alpha_k \quad (24)$$

for displacements in the x-direction of Fig. 8, $k = 1, 2, \ldots$, and by

$$u_y(x, y) = \alpha_k \quad (25)$$

for displacements along the y-lines of the diffraction grating.

As described earlier, the moiré interferometry hole-drilling experiments produce images of iso-displacement contours. It would, therefore, be useful to generate contour plots theoretically using eqs (24) and (25) and compare such theoretical contour plots with the moiré images from the experiments. However, eqs (22) and (23) do not take into account the nonzero optical mismatch that is present in the moiré images.

The optical mismatch in the moiré images arises from the mismatch between the spacing of the furrows in the diffraction grating on the test specimen and the spacing in the virtual grating produced by the two interfering laser beams. In essence, mismatch is an optical phenomenon that does not reflect the reality of the state of deformation at the surface of the test specimen, but is superposed onto the contour plots that would be obtained with eqs (22)-(25). Thus, the optical system produces straight, equally spaced parallel fringe lines in the moiré image even in the case of a test specimen with an undeformed diffraction grating, that is, before any holes are drilled. The mismatch, measured as the number of mismatch fringes per inch of image, can be changed by making adjustments in the experimental equipment.

To avoid analytically formulating the mathematics of the optics of the moiré interferometry equipment, we proposed that the mismatch be considered equivalent to two constant strain fields $\varepsilon_x^{\text{MISMATCH}}$ and $\varepsilon_y^{\text{MISMATCH}}$ that can be linearly superposed into the theory of elasticity formulations.

These mismatch strain fields are calculated as

$$\varepsilon_x^{\text{MISMATCH}} = (X - \text{mismatch}) \cdot (\text{moiré sensitivity}) \quad (26)$$

$$\varepsilon_y^{\text{MISMATCH}} = (Y - \text{mismatch}) \cdot (\text{moiré sensitivity}), \quad (27)$$

where the X mismatch is the number of mismatch fringes per inch counted along the X-axis and the Y mismatch is the number of mismatch fringes per inch counted along the Y-axis. Superposition of these mismatch strains results in eqs (22) and (23) being modified to

$$u_x = u_x^{(1)} - u_x^{(2)} + \varepsilon_x^{\text{MISMATCH}} \cdot x \quad (28)$$

$$u_y = u_y^{(1)} - u_y^{(2)} + \varepsilon_y^{\text{MISMATCH}} \cdot y. \quad (29)$$

When eqs (28) and (29) are used with eqs (11)-(16), (20), (21), (24) and (25) to generate the theoretical contour plots, excellent agreement is found between theory and experiment.

One can envision plotting contour lines for the x displacement using

$$u_x^{(1)}(x, y) - u_x^{(2)}(x, y) + \varepsilon_x^{\text{MISMATCH}} \cdot x = \alpha_k, \quad (30)$$

which results from combining eqs (24) and (28), or

$$u_x^{(1)}(x, y) - u_x^{(2)}(x, y) = \alpha_k, \quad (31)$$

which results from combining eqs (22) and (24), or simply,

$$u_x^{(1)}(x, y) = \alpha_k. \quad (32)$$

Similar equations can be written for the y displacement. Note that in general, eqs (30)-(32) are very complicated. In certain cases, an analytical, explicit function f or g can be found such that $y = f(x)$, or $x = g(y)$, identically satisfies one of eqs (30)-(32).

One such case occurs when $\sigma_1 = \sigma_2$, which is the situation throughout the plug of the circular test specimen. The contour line for eq (32) is given explicitly by

$$y = \pm\sqrt{x \cdot \frac{\left[x^2 - \frac{2E\alpha_k}{(\sigma_1+\sigma_2)(1-\nu)} \cdot x + \frac{b^2(1+\nu)}{1-\nu}\right]}{\left[\frac{2E\alpha_k}{(\sigma_1+\sigma_2)(1-\nu)} - x\right]}}. \quad (33)$$

Equation (33) is plotted in Fig. 9 for 40 values α_k of the x displacement ($k = 1, \ldots, 40$). The constants used in Fig. 9 are $\sigma_1 = \sigma_2 = -32831$ psi, $E = 10.3 \times 10^6$ psi, $\nu = 0.33$ and $b = 0.032$ in. The contour lines for the y displacement in Fig. 10 are identical in shape to those of Fig. 9. This is because the state of stress is symmetric. In Figs. 9 and 10, the slopes of almost all of the contour lines shown approach either zero or infinity as $x \to \pm\infty$ or $y \to \pm\infty$.

Note from Figs. 9 and 10 that for certain values of α_k, there exist more than one contour line. This is shown more clearly in Fig. 11. Figure 11 was plotted for $\sigma_1 = \sigma_2 = 4506$ psi, $E = 10.3 \times 10^6$ psi, $\nu = 0.30$ and $b = 0.030$ in. This means that the x displacement does not monotonically increase as one moves away from the edge of the hole. Rather, it first decreases, reaches a minimum at a certain radial distance r^*, and then increases. The location of this minimum value of $u_x^{(1)}$ as one moves along the x-axis—that is, for $\theta = \varphi$, can

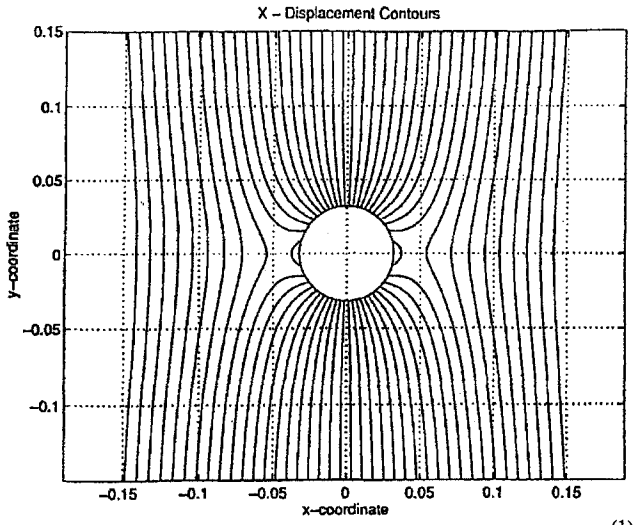

Fig. 9—Theoretical contour plot for total X displacement $u_x^{(1)}$ in the case of $\sigma_1 = \sigma_2 = -32831$ psi (without mismatch)

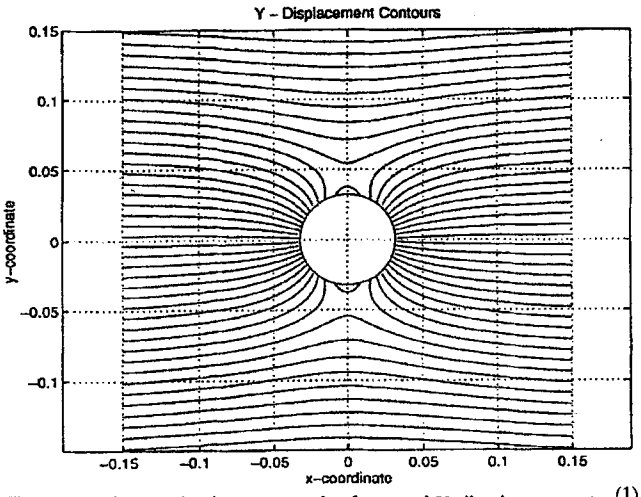

Fig. 10—Theoretical contour plot for total Y displacement $u_y^{(1)}$ in the case of $\sigma_1 = \sigma_2 = -32831$ psi (without mismatch)

be easily determined with calculus from eqs (11), (12) and (15) as

$$r^* = b\sqrt{\frac{1+\nu}{1-\nu}}. \tag{34}$$

Note from eq (34) the role that the Poisson ratio plays in this phenomenon of multiple contour lines. According to eq (34), for $\nu = 0.33$, $r = 1.41b$, where b is the radius of the drilled hole, whereas for $\nu = 0$, there is no such relative minimum point.

Radically different contour plots can be obtained with eq (31). For the biaxial state of stress $\sigma_1 = \sigma_2$, the explicit form of eq (31) is

$$y = \pm\sqrt{x \cdot \left[\frac{(\sigma_1+\sigma_2)(1+\nu)b^2}{2E\alpha_k} - x\right]}. \tag{35}$$

Equation (35) is plotted in Fig. 12 for 40 values α_k of the x displacement ($k = 1, \ldots, 40$). It can be shown that each contour line is part of a circle, which is tangent to the vertical

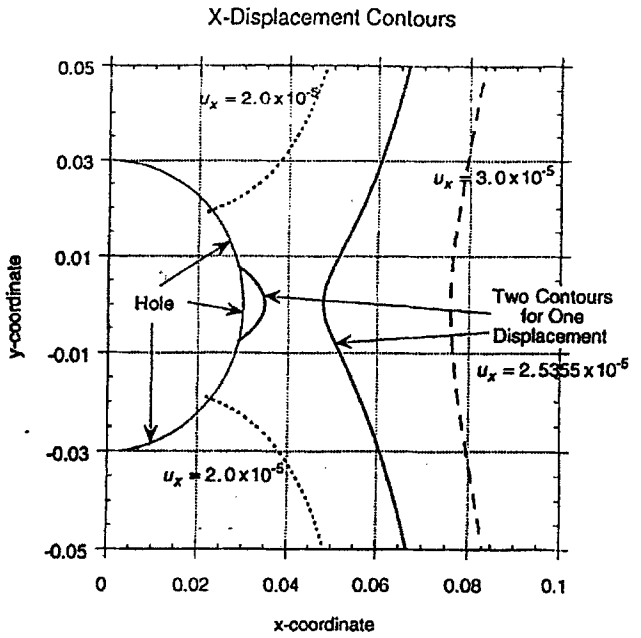

Fig. 11—Multiple contour lines for total X displacement $u_x^{(1)}$ in the case of $\sigma_1 = \sigma_2 = -4506$ psi (without mismatch)

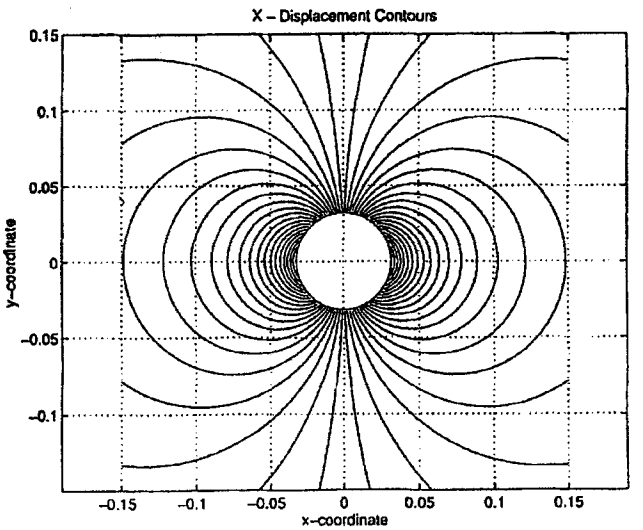

Fig. 12—Theoretical contour plot for relative X displacements $[u_x^{(1)} - u_x^{(2)}]$ in the case of $\sigma_1 = \sigma_2 = -32831$ psi (without mismatch)

y-axis and has a radius ρ of

$$\rho = \frac{(\sigma_1+\sigma_2)(1+\nu)b^2}{4E\alpha_k}. \tag{36}$$

The contour lines for the y displacement are plotted in Fig. 13, and are identical in shape to the x-displacement contour lines described by eq (35).

Software for Generating Contour Plots

In general, eqs (30)-(32) cannot be solved explicitly in a form $y = f(x)$ or $x = g(y)$, and special contour generation algorithms and software are required. Initially, a FORTRAN computer program was written on a workstation that would numerically calculate tables of (x, y) coordinates that satisfy either eq (24) or eq (25). These tables would in turn be plotted

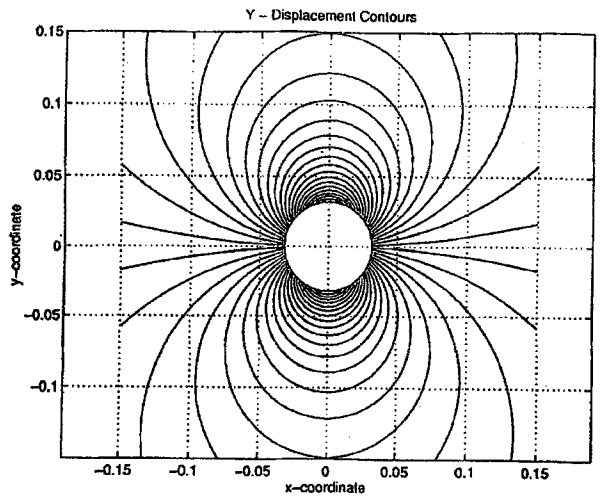

Fig. 13—Theoretical contour plot for relative Y displacements $[u_y^{(1)} - u_y^{(2)}]$ in the case of $\sigma_1 = \sigma_2 = -32831$ psi (without mismatch)

on a Macintosh computer. In the final version of this program, explicit, finite difference integration was used to obtain each contour line. Denoting eqs (24) and (25) collectively as

$$h(x, y) = \alpha_k, \tag{37}$$

the iterative, contour-generating equations were

$$x_{j+1} = x_j + \frac{\frac{\partial h}{\partial y}}{\sqrt{\left(\frac{\partial h}{\partial x}\right)^2 + \left(\frac{\partial h}{\partial y}\right)^2}} \cdot \Delta s \tag{38}$$

$$y_{j+1} = y_j - \frac{\frac{\partial h}{\partial x}}{\sqrt{\left(\frac{\partial h}{\partial x}\right)^2 + \left(\frac{\partial h}{\partial y}\right)^2}} \cdot \Delta s, \tag{39}$$

where $j = 0, 1, 2, \ldots$. The partial derivatives $\partial h/\partial x$ and $\partial h/\partial y$ were evaluated at the point (x_j, y_j). [Note that expressions for the eight partial derivatives of u_r, u_θ, u_x and u_y with respect to r and θ are required to evaluate the four partial derivatives of u_x and u_y with respect to x and y in eqs (38) and (39).] The quantity Δs stands for the increment in the arc length of the contour line, chosen by the computer program to be a tiny fraction of the geometric dimensions of the problem. The initial condition (x_0, y_0) for eqs (38) and (39) would have to satisfy eq (37), and was determined by another algorithm. For each contour line k, eqs (38) and (39) would result in a finite series of points (x_0, y_0), (x_1, y_1), (x_2, y_2), ... that would satisfy eq (37). The contour lines were plotted from a subset of points constructed by the computer program from each series, since typically the series generated by eqs (38) and (39) would contain thousands of points to maintain the accuracy of the numerical integration. Nevertheless, the computation times on the workstation were trivial.

Note that an unsuccessful attempt was also made at using the Newton-Raphson method to obtain contour lines for eq (37). In this approach, for a given finite set of x_j (or y_j), $j = 0, 1, 2, \ldots$, the nonlinear eq (36) in the variable y (or x) was solved holding $x = x_j$ (or $y = y_j$), and we obtained the corresponding y_j (or x_j) after several iterations. The resulting finite set of points (x_j, y_j), $j = 0, 1, 2, \ldots$, would form a contour line k.

Many interesting phenomena in the contour plots were discovered during this stage of the simulation/analysis effort, some of which proved too difficult to handle with the finite difference contour generation program. One such difficulty was the phenomenon of multiple contour lines described in the previous section. Eventually, the contour-plotting capabilities of the MATLAB program[14] were discovered, and an M-file in the MATLAB language was written for generating contour plots of the complicated displacement functions discussed above.

MATLAB has proven to be effective in generating the contour plots for the moiré images in this work, and it is easy to use. The following information is included in the input data of the M-file:

1. the range $x_p \le x \le x_q$, $y_p \le y \le y_q$ in the x-y plane over which the contour plots are to be generated;
2. the number of grid points in the x-y plane defined through input variables Δx and Δy;
3. the values of E, ν, b, φ, σ_1, σ_2, $\varepsilon_x^{\text{MISMATCH}}$ and $\varepsilon_y^{\text{MISMATCH}}$;
4. in eqs (28) and (29), whether $u_x^{(2)} \equiv 0$ and $u_y^{(2)} \equiv 0$;
5. in eqs (28) and (29), whether $\varepsilon_x^{\text{MISMATCH}} \equiv 0$ and $\varepsilon_y^{\text{MISMATCH}} \equiv 0$;
6. the number of contour lines to be included in the ranges $x_p \le x \le x_q$, $y_p \le y \le y_q$ (this defines the X mismatch and the Y mismatch);
7. the values of α_k in eqs (24) and (25).

Once the MATLAB system and the M-file are called, prompts for the input described above are received on the monitor screen. The contour plots for the x and y displacements appear on the screen after a few minutes of computation on the workstation.

Using MATLAB for eq (32), the contour plot of Fig. 14(a) for the total x displacement is obtained for the following constants: $\sigma_1 = -43.99$ MPa, $\sigma_2 = 64.81$ MPa, $E = 71.0$ GPa, $\nu = 0.33$, $b = 0.81$ mm and $\varphi = -30$ deg. These values correspond to hole 8, which was described earlier. Figure 14(b) is the analogous contour plot for the total y displacement, and both Figs. 14(a) and 14(b) were plotted for 40 values of the displacement.

An example of the theoretical fringe patterns for hole 8 is presented as Figs. 14(a) and 14(b). An examination of the theoretical fringe patterns for holes 5, 6, 8 and 11, which were also off-axis holes, showed the average angle of rotation of fringe symmetry at the hole boundary to be closely equal to the principal strain angle. Table 4 shows a comparison of the theoretical principal strain angles obtained by the mathematically generated plots and those measured in our experiments. The correlation was excellent.

Conclusions

The moiré interferometric hole-drilling method can be applied to cases in which the actual principal strain axes are not

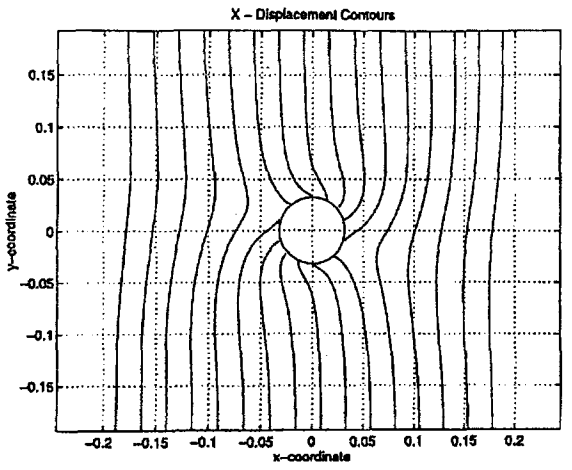

(a)

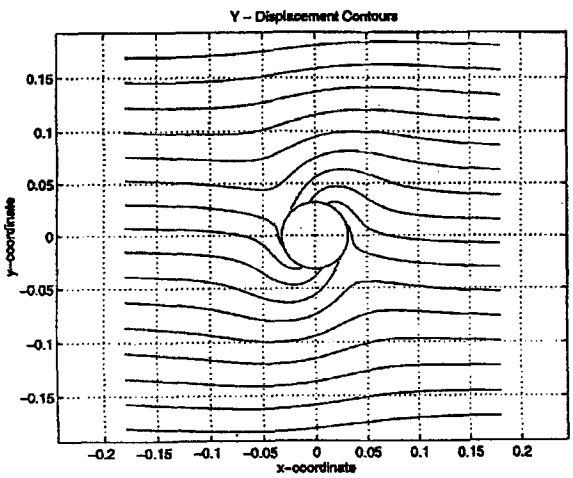

(b)

Fig. 14—Theoretical isothetic contour plots of the X displacements (radial), hole 8, and (b) Y displacements (tangential), hole 8

aligned with the installed grid axes. Grids of 1200 lines/mm or greater should be applied to the test article to maximize the resolution of the system.

References

1. Proceedings of the Fourth International Conference on Residual Stress, Society for Experimental Mechanics, Bethel, CT (June 1994).

2. ASTM E837-95, "Standard Test Method for Determining Residual Stresses by the Hole-drilling Strain-gage Method," Annual Book of Standards, American Society for Testing and Materials, Philadelphia (1998).

3. Post, D., "Moiré Interferometry at VPI&SU," EXPERIMENTAL MECHANICS, **23**, *203–210 (June 1983).*

4. McDonach, A., MacKenzie, P.M., McKelvie, J., and Walker, C.A., "Measurement of Residual Stresses by a Moiré Fringe Method with Hole Drilling, and Verification on Titanium Compressor Ring," Proceedings of the 1990 SEM Spring Conference on Experimental Mechanics, 765–768 (June 1990).

5. Nicolletto, G., "Moiré Interferometry Determination of Residual Stress in the Presence of Gradients," EXPERIMENTAL MECHANICS, **31**, *252–256 (Sep. 1991).*

6. Livnat, A. and Post, D., "The Grating Equations for Moiré Interferometry and Their Identity to Equations of Geometrical Moiré," EXPERIMENTAL MECHANICS, **25**, *360–366 (Dec 1985).*

7. Post, D., "Moiré Interferometry," Handbook on Experimental Mechanics, A.S. Kobayashi, ed., Prentice Hall, Englewood Cliffs, NJ (1987).

8. Soete, W. and Vancrombrugge, R., "An Industrial Method for the Determination of Residual Stresses," 1949 SEM Spring Conference on Experimental Mechanics, 17–28 (1949).

9. Weissman, E.M. and Post, D., "The Full Field Displacement and Strain Rosettes by Moiré Interferometry," EXPERIMENTAL MECHANICS, **22**, *324–328 (1982).*

10. Wang, C.-T., Applied Elasticity, McGraw-Hill, New York (1953).

11. Parks, V.J., "Geometric Moiré," Handbook on Experimental Mechanics, A.S. Kobayashi, ed., Prentice Hall, Englewood Cliffs, NJ (1987).

12. Flügge, W., Handbook of Engineering Mechanics, McGraw-Hill, New York (1962).

13. Timoshenko, S.P. and Goodier, J.N., Theory of Elasticity, McGraw-Hill, New York (1970).

14. MATLAB User's Guide, The MathWorks Inc., Natick, MA (1991).